

# A Deformable Slider Joint for Multibody Applications

Stefania Gualdi, Marco Morandini and Pierangelo Masarati  
*Dipartimento di Ingegneria Aerospaziale, Politecnico di Milano*

## Abstract

This paper presents the implementation of a deformable slider joint in the framework of a multibody simulation environment. A slider joint constrains the motion of a rigid body point along a line: a deformable slider joint allows the constrained point to move along a series of deformable beams, switching from one to the other without encountering serious numerical discontinuities. The behavior of the deformable slider is influenced both by the slider constraint and by the beam formulation, as the slider introduces a concentrated load at arbitrary points along the beam. This joint element proves to be fundamental in the study of telescopic landing gear dynamics. In fact, an application concerning the spring-back phenomena clearly demonstrates the importance of correctly modeling the strut deformability.

## 1 Introduction

Different types of slider joints can be formulated, namely the “spherical”, the “classical” and the “spline” slider. The first imposes no constraint on the relative rotations of the rigid body, the second enforces constraints on the rigid body rotation components in the line normal plane, while the last differs from the “classical” case by imposing the body orientation also with respect to the component along the line direction. The importance of an appropriate formulation of the slider constraint has been recently highlighted in [1].

The slider joint presented in this paper has been implemented in the framework of an open source multibody analysis code named MBDyn, developed at the Department of Aerospace Engineering of the University “Politecnico di Milano”, and currently used in the simulation of rotorcraft and aircraft dynamics [2, 3, 4, 5].

This constraint has been introduced in order to account for the behavior of particular mechanical elements, such as the piston-cylinder arrangements of landing gear shock absorbers, where the effects of deformation on the relative motion between parts can be crucial [6, 7]. The analytical formulation of the deformable slider joint has to be slightly modified to account for the peculiar beam formulation adopted in MBDyn. In fact, the beam elements currently implemented in this multibody code are derived from a finite volume formulation [8]. The weak form of the equilibrium equations in this case is obtained by means of piecewise constant value test functions centered on each structural node. This leads to severe discontinuities when the sliding body switches from the area of influence of one node to that of another. The discontinuities are recovered by “spreading” the contact area of the joint over a finite beam length, as occurs in reality. Furthermore, the effect of the application of a force at an arbitrary point along the beam must be carefully analyzed, because the response of the system can be quite different from that originated by a nodal force.

Numerical examples illustrating the static behavior of two deformable beams constrained to one another by two sliders are presented. The effects of the slider relative motion on the overall system stiffness are evident from simulation results. Finally, an application of the slider joint in a landing gear model is presented. In this particular case, the joint allows a precise simulation of the relative motion between the piston and cylinder of the shock absorber, and the loads exchanged between the two elements are readily recovered.

## 2 Multibody Framework

The slider joint that is presented in the following sections has been implemented in the MBDyn multibody/multi-disciplinary dynamics analysis framework, which is developed at the Dipartimento di Ingegneria Aerospaziale of the University “Politecnico di Milano”. It is publicly available at <http://www.aero.polimi.it/~mbdyn/> in source form. MBDyn is an initial value problem solver with a set of libraries that allow to model mechanical, aeroelastic, hydraulic systems and generic circuits for control purposes. User-defined elements can be easily added both by patching the code or by writing runtime loadable objects.

The problem is written as a system of Differential-Algebraic Equations (DAE), where the differential equations model the dynamics of the system, while the algebraic ones represent kinematic constraints.

The solution is currently computed by means of an original multistep integration algorithm for the prediction [9], and a *Newton-Raphson* correction iteration; current development is focusing on more sophisticated and performing approaches.

### 3 Slider Constraint

A slider is a joint that constrains the motion of a point along a line. The orientation of the body associated to the point may be constrained as well. Three different types of slider are worth considering: (a) the one that will be called the “spherical” slider, which implies no constraints on the orientation of the sliding body, (b) the one that will be called the “classical” slider, which implies a constraint on the orientation of the body with respect to the plane that is normal to the line, and (c) the one that will be called the “spline” slider, which enforces an additional constraint on the orientation of the body about the direction of the line (e.g. a screw).

Consider a  $C^1$  line  $\mathbf{x}$  in a three-dimensional space; let  $\xi$  be an abscissa along the line. The direction of the line at an arbitrary point,  $\mathbf{t}$ , is defined as the normalized gradient of the line with respect of the abscissa  $\xi$ , namely:  $\mathbf{t} = \mathbf{l} / \|\mathbf{l}\|$ , with  $\mathbf{l} = \mathbf{x}_{/\xi}$ . The regularity assumption implies that  $\mathbf{l}$  and  $\mathbf{t}$  be continuous. The direction  $\mathbf{t}$  implicitly defines a plane normal to the line. The configuration of the sliding body is identified by its position,  $\mathbf{x}_b$ , and orientation,  $\mathbf{R}_b$ .

#### 3.1 Position Constraint

All the types of slider joint that are considered require the position of the point to be on the line:

$$\mathbf{x}_b - \mathbf{x}(\xi) = 0, \quad (1)$$

which is a three-dimensional algebraic constraint equation. However, the abscissa  $\xi$  of the contact point is generally unknown, so it must be determined by solving a nonlinear problem, consisting in the projection of Equation (1) in the plane normal to the direction  $\mathbf{t}$  at point  $\mathbf{x}(\xi)$ , i.e.  $(\mathbf{I} - \mathbf{t} \otimes \mathbf{t}) \cdot (\mathbf{x}_b - \mathbf{x}(\xi)) = 0$ , resulting in

$$-\mathbf{t} \times \mathbf{t} \times (\mathbf{x}_b - \mathbf{x}(\xi)) = 0. \quad (2)$$

Consider two directions,  $\mathbf{e}_2$  and  $\mathbf{e}_3$ , mutually orthogonal and orthogonal to  $\mathbf{t}$ ; the three directions form an orientation matrix  $\mathbf{R} = [\mathbf{t} \ \mathbf{e}_2 \ \mathbf{e}_3]$  that can be used to project the constraint of Equation (2) in the plane normal to the line at point  $\xi$ :

$$-\mathbf{R}^T \cdot \mathbf{t} \times \mathbf{t} \times (\mathbf{x}_b - \mathbf{x}(\xi)) = 0;$$

of course the projection in direction  $\mathbf{t}$  vanishes, and the two remaining equations are

$$\begin{aligned} \mathbf{e}_2 \cdot (\mathbf{x}_b - \mathbf{x}(\xi)) &= 0, \\ \mathbf{e}_3 \cdot (\mathbf{x}_b - \mathbf{x}(\xi)) &= 0. \end{aligned}$$

The problem can be automatically and simultaneously solved by directly using Equation (1), adding the contact point abscissa  $\xi$  to the set of unknowns.

The constraint results in a reaction force whose components lie in the plane normal to the direction  $\mathbf{t}$ .

If a hypothetical virtual work function is augmented with the constraint equations following the *lagrangian multipliers* approach, one obtains  $L^* = \boldsymbol{\lambda} \cdot (\mathbf{x}_b - \mathbf{x}(\xi))$ , where  $\boldsymbol{\lambda}$  are the multipliers that directly represent the reaction forces in the global system, since they are conjugate to the global displacement constraint. The virtual perturbation of the augmenting function yields

$$\delta L^* = \delta \boldsymbol{\lambda} \cdot (\mathbf{x}_b - \mathbf{x}(\xi)) + \delta \mathbf{x}_b \cdot \boldsymbol{\lambda} - \delta \xi \mathbf{x}_{/\xi} \cdot \boldsymbol{\lambda}, \quad (3)$$

because the virtual perturbation of the curve at point  $\xi$  results in  $\delta \mathbf{x}(\xi) = \delta \xi \mathbf{x}_{/\xi}$ , as the contact point is the only unknown. The resulting equation,  $\mathbf{l} \cdot \boldsymbol{\lambda} = 0$ , requires the reaction force  $\boldsymbol{\lambda}$  to be orthogonal to the line at abscissa  $\xi$ ; it is the term that actually ensures the constraint is applied at the appropriate point along the line.

### 3.2 Orientation Constraint: “Classical” Slider

If the point has a structure, its orientation may be affected by the constraint. In fact the entity that is being constrained is no longer a point: it is a body. The so-called “classical” slider is considered first. Its orientation with respect to two arbitrary directions lying in the plane orthogonal to the direction  $\mathbf{t}$  and mutually orthogonal is constrained. Assuming that direction 1 in the frame attached to the body is oriented as the line at the contact point,  $\mathbf{x}(\xi)$ , two orthogonality relationships can be written between the direction of the line and the directions  $\mathbf{e}_{b2}$  and  $\mathbf{e}_{b3}$  of the frame of the body:

$$\begin{aligned}\mathbf{e}_{b2} \cdot \mathbf{t} &= 0, \\ \mathbf{e}_{b3} \cdot \mathbf{t} &= 0.\end{aligned}$$

The constraint equations can be de-normalized by using the gradient of the line,  $\mathbf{l}$ , instead of the direction  $\mathbf{t}$ :

$$\begin{aligned}\mathbf{e}_{b2} \cdot \mathbf{l} &= 0, \\ \mathbf{e}_{b3} \cdot \mathbf{l} &= 0.\end{aligned}$$

The constraint reactions act about the axes determined by the cross-product between the two directions  $\{\mathbf{e}_{b2}, \mathbf{e}_{b3}\}$  and the direction of the line. Their contribution to the dynamics of the body results from considering the following augmentation of the virtual work of the system:

$$L^* = \mu_2 \mathbf{e}_{b2} \cdot \mathbf{l} + \mu_3 \mathbf{e}_{b3} \cdot \mathbf{l},$$

where  $\{\mu_2, \mu_3\}$  are scalar multipliers related to the reacting couples generated by the constraint. The virtual perturbation of the augmented work function yields

$$\delta L^* = \delta \mu_2 \mathbf{e}_{b2} \cdot \mathbf{l} + \delta \mu_3 \mathbf{e}_{b3} \cdot \mathbf{l} + \boldsymbol{\theta}_{b\delta} \cdot ((\mathbf{e}_{b2} \mu_2 + \mathbf{e}_{b3} \mu_3) \times \mathbf{l}) + \delta \xi \mathbf{l}_{/\xi} \cdot (\mathbf{e}_{b2} \mu_2 + \mathbf{e}_{b3} \mu_3), \quad (4)$$

where  $\boldsymbol{\theta}_{b\delta}$  is the vector characterizing the skew tensor  $\delta \mathbf{R}_b \mathbf{R}_b^T$ , namely  $\boldsymbol{\theta}_{b\delta} = \text{ax}(\delta \mathbf{R}_b \mathbf{R}_b^T)$ . Each contribution to the reacting couple is given by  $(\mathbf{e}_{bj} \times \mathbf{l}) \mu_j$ , with the scalar couple  $\mu_j$  acting about direction  $\mathbf{e}_{bj} \times \mathbf{l}$ . The perturbation of the gradient of the line,  $\mathbf{l}$ , is

$$\delta \mathbf{l} = \delta \xi \mathbf{l}_{/\xi},$$

in analogy with the perturbation of the contact point position. Note that  $\mathbf{l}_{/\xi}$  is the *curvature* of the line, which in general differs from the notion of *beam curvature* in the sense of the orientation gradient of a beam section.

### 3.3 Orientation Constraint: “Spline” Slider

The “spline” constraint requires a relationship to hold between the orientation of the body and the line in the direction of the line itself. In this case, a model of the line is not enough; it needs a structure, i.e. an orientation must be associated with every point of the line. A frame  $\mathbf{R}(\xi)$  is defined, that describes a structure for the line. For the sake of generality, there is no explicit relationship between direction 1 of such a frame and the direction of the line,  $\mathbf{t}$ . It is simply assumed that their scalar product is not null and positive:  $\mathbf{e}_1 \cdot \mathbf{t} > 0$ . We are mostly interested in how the orientation  $\mathbf{R}(\xi)$  varies along the line, to establish a relationship between this change and the change in orientation of the body. The relative orientation between the body and the frame on the line is

$$\mathbf{R}_\Delta = \mathbf{R}_b \mathbf{R}^T$$

According to the definition of the constraint, the component of the relative orientation in the direction of the line must be null at all times. The relative orientation, defined by a vector  $\boldsymbol{\phi} = \mathbf{v}\varphi$ , of amplitude  $\varphi$  and direction  $\mathbf{v}$ , yields

$$\mathbf{R}_\Delta(\boldsymbol{\phi}) = \mathbf{I} + \sin(\varphi) \mathbf{v} \times + (1 - \cos(\varphi)) \mathbf{v} \times \mathbf{v} \times .$$

If the amplitude is small, as in this case, in which it must be zero, the vector  $\boldsymbol{\phi}$  can be approximated with the vector that yields the skew symmetric part of the relative orientation matrix, given by the *axial* operator,  $\text{ax}(\cdot)$ :

$$\boldsymbol{\phi} \cong \text{ax}(\mathbf{R}_\Delta) = \sin(\varphi) \mathbf{v}.$$

The constraint equation states that the relative orientation vector must be orthogonal to the line:

$$\boldsymbol{\phi} \cdot \boldsymbol{t} = 0,$$

or, if the equation is de-normalized by considering the gradient of the line itself,  $\boldsymbol{l}$ :

$$\boldsymbol{\phi} \cdot \boldsymbol{l} = 0.$$

Again, the augmented work function becomes  $L^* = \mu_1 \boldsymbol{\phi} \cdot \boldsymbol{l}$ , where  $\mu_1$  is a scalar multiplier; the virtual perturbation yields

$$\delta L^* = \delta \mu_1 \boldsymbol{\phi} \cdot \boldsymbol{l} + \boldsymbol{\theta}_{b\delta} \cdot \boldsymbol{l} \mu_1 + \delta \xi \boldsymbol{l}_{/\xi} \cdot \boldsymbol{\phi} \mu_1. \quad (5)$$

This contribution must be added to the equations of the ‘‘classical’’ slider. There is a strong similarity between this equation and Equation (4), which describes the ‘‘classical’’ constraint; however, in the present case the *relative* orientation between the body and the structure of the line is considered, whereas in the former one the *absolute* orientation of the body is used. The virtual perturbation of the relative orientation results in the virtual perturbation of the orientation of the body:  $\delta \boldsymbol{\phi} = \boldsymbol{\theta}_{b\delta}$ ; this results from perturbing the *axial* operator.

## 4 Deformable Slider Constraint

In the previous paragraph the equations that describe the kinematics of a body sliding on a (structured) rigid line were discussed. The problem can be generalized to the case of a deformable line, whose position, and orientation, depends on some degrees of freedom of the problem.

In this case, the line is attached to a beam, a slender deformable element that is described by means of a reference line and a reference orientation mapped on the same domain as the line, that describes the orientation of the beam section. The main difference occurs in the virtual perturbation of the line and of its orientation. The virtual perturbation of the position of the line becomes

$$\delta \boldsymbol{x}(\xi) = \delta \{q\}^T \frac{\partial \boldsymbol{x}}{\partial \{q\}} + \delta \xi \boldsymbol{x}_{/\xi},$$

where  $\{q\}$  are the (discrete) unknowns that describe the configuration of the beam. They can represent some modal amplitude unknowns or nodal position and orientation parameters. The virtual perturbation of the gradient of the line becomes

$$\delta \boldsymbol{l} = \delta \{q\}^T \frac{\partial \boldsymbol{l}}{\partial \{q\}} + \delta \xi \boldsymbol{l}_{/\xi}.$$

The virtual perturbation of the orientation of the line, when perturbing the relative orientation of the ‘‘spline’’ slider, in an analogous manner yields

$$\delta \boldsymbol{\phi} = \boldsymbol{\theta}_{b\delta} - \boldsymbol{R}_\Delta \cdot \boldsymbol{\theta}_\delta,$$

where  $\boldsymbol{\theta}_\delta$  is the *axial* of the skew tensor  $\delta \boldsymbol{R} \boldsymbol{R}^T$ ; it is equal to

$$\boldsymbol{\theta}_\delta = \delta \{q\}^T \frac{\partial \boldsymbol{\theta}}{\partial \{q\}} \cdot \boldsymbol{\Gamma}^T + \delta \xi \boldsymbol{k},$$

where the tensor  $\boldsymbol{\Gamma}(\boldsymbol{\theta})$  is defined in such a way that  $\boldsymbol{\theta}_\delta = \boldsymbol{\Gamma} \cdot \delta \boldsymbol{\theta}$  and the curvature vector  $\boldsymbol{k}$  measures the change of orientation along the beam, i.e.  $\boldsymbol{k} = ax \left( \boldsymbol{R}_{/\xi} \boldsymbol{R}^T \right)$ .

The virtual perturbation of the augmented work becomes: (a) for the position constraint of Equation (3),

$$\delta L^* = \delta \boldsymbol{\lambda} \cdot (\boldsymbol{x}_b - \boldsymbol{x}(\xi)) + \delta \boldsymbol{x}_b \cdot \boldsymbol{\lambda} - \delta \{q\}^T \frac{\partial \boldsymbol{x}}{\partial \{q\}} \cdot \boldsymbol{\lambda} - \delta \xi \boldsymbol{x}_{/\xi} \cdot \boldsymbol{\lambda},$$

that defines the “spherical” slider and is common to all the types of joint; (b) for the “classical” slider orientation constraint of Equation (4)

$$\begin{aligned}\delta L^* &= \delta\mu_2 \mathbf{e}_{b2} \cdot \mathbf{l} + \delta\mu_3 \mathbf{e}_{b3} \cdot \mathbf{l} + \boldsymbol{\theta}_{b\delta} \cdot ((\mathbf{e}_{b2} \mu_2 + \mathbf{e}_{b3} \mu_3) \times \mathbf{l}) \\ &\quad + \delta\{q\}^T \frac{\partial \mathbf{l}}{\partial \{q\}} \cdot (\mathbf{e}_{b2} \mu_2 + \mathbf{e}_{b3} \mu_3) + \delta\xi \mathbf{l}_{/\xi} \cdot (\mathbf{e}_{b2} \mu_2 + \mathbf{e}_{b3} \mu_3); \end{aligned}$$

and (c) for the “spline” slider orientation constraint of Equation (5)

$$\delta L^* = \delta\mu_1 \boldsymbol{\phi} \cdot \mathbf{l} + \boldsymbol{\theta}_{b\delta} \cdot \mathbf{l} \mu_1 - \delta\{q\}^T \frac{\partial \boldsymbol{\theta}}{\partial \{q\}} \cdot \boldsymbol{\Gamma}^T \mathbf{R}_\Delta^T \cdot \mathbf{l} \mu_1 - \delta\xi \mathbf{k} \cdot \mathbf{R}_\Delta^T \cdot \mathbf{l} \mu_1 + \delta\{q\}^T \frac{\partial \mathbf{l}}{\partial \{q\}} \cdot \boldsymbol{\phi} \mu_1 + \delta\xi \mathbf{l}_{/\xi} \cdot \boldsymbol{\phi} \mu_1.$$

that is considered in addition to the “classical” slider constraint equation.

## 5 Finite Volume Implementation

As briefly mentioned in the introduction, the behavior of a beam element subject to an arbitrarily positioned force has to be carefully evaluated in order to assess the global performance of the slider constraint. In fact, the slider constraint formulation is strongly coupled with the beam formulation. This paper focuses on the application of the slider constraint to a finite volume beam model [8]. In short, the beam element is divided in finite influence regions surrounding the nodes. The boundaries between the influence regions are the so-called *evaluation points*. Optimal evaluation point placement results in accurate and shear lock-free beam behavior. For two-node beam elements, the optimal placement is at mid-point; for three-node beam elements, the optimal placement is in the third-order accurate *Gauss* integration points, e.g.  $s = \pm 1/\sqrt{3}$  when the nondimensional beam extremities are in  $\{-1, 1\}$ . To characterize the coupling in the case of a finite volume formulation, the analytical solution for a clamped beam, in terms of tip displacement, tip rotation and internal forces and moments at the evaluation points, is compared to the results obtained for two- and three-node finite volume beams.

### 5.1 Exact Solution

Consider a straight, untwisted uniform beam. The displacement and the rotation at  $\xi = L$ , resulting from a concentrated force,  $F$ , applied at station  $0 \leq \xi \leq L$ , i.e. ranging from the clamped node, in  $\xi = 0$ , to the free node in  $\xi = L$ , are:

$$\begin{aligned}v(L) &= F \left( \frac{\xi^2}{6EJ} (3L - \xi) + \frac{\xi}{GA} \right) \\ \phi(L) &= F \frac{\xi^2}{2EJ}\end{aligned}$$

The internal forces and moments at an arbitrary point  $\zeta$  are:

$$\begin{aligned}S(\zeta) &= F \text{step}(\xi - \zeta) \\ M(\zeta) &= F \text{ramp}(\xi - \zeta)\end{aligned}$$

### 5.2 Two-Node Finite Volume Beam

This beam element has not been interfaced to the slider joint in MBDyn; its behavior is reported only to provide an insight into the properties of the finite volume beam formulation. The tip displacement and rotation, resulting from a concentrated force,  $F$ , applied at station  $0 \leq \xi \leq L$ , become

$$\begin{aligned}v(L) &= F \left( \frac{L^2}{2EJ} \left( \xi - \frac{L}{2} \right) + \frac{L}{GA} \right) \text{step} \left( \xi - \frac{L}{2} \right) \\ \phi(L) &= F \frac{L}{EJ} \text{ramp} \left( \xi - \frac{L}{2} \right)\end{aligned}$$

The internal forces and moments at the evaluation point (mid-point) are:

$$\begin{aligned} S\left(\frac{L}{2}\right) &= F_{\text{step}}\left(\xi - \frac{L}{2}\right) \\ M\left(\frac{L}{2}\right) &= F_{\text{ramp}}\left(\xi - \frac{L}{2}\right) \end{aligned}$$

### 5.3 Three-Node Finite Volume Beam

The tip displacement and rotation, resulting from a concentrated force,  $F$ , applied at station  $L(1 + 1/\sqrt{3})/2 \leq \xi \leq L$ , are:

$$\begin{aligned} v(L) &= F\left(\frac{L^2}{6EJ}(3\xi - L) + \frac{L}{GA}\right) \\ \phi(L) &= F\frac{L}{EJ}\left(\xi - \frac{L}{2}\right) \end{aligned}$$

The internal forces and moments at the evaluation point at  $\xi = L(1 + 1/\sqrt{3})/2$  are:

$$\begin{aligned} S\left(\frac{L}{2}\left(1 + \frac{1}{\sqrt{3}}\right)\right) &= F \\ M\left(\frac{L}{2}\left(1 + \frac{1}{\sqrt{3}}\right)\right) &= F\left(\xi - \frac{L}{2}\left(1 + \frac{1}{\sqrt{3}}\right)\right) \end{aligned}$$

The corresponding displacements and rotations when the force is applied in  $L(1 - 1/\sqrt{3})/2 \leq \xi \leq L(1 + 1/\sqrt{3})/2$ , i.e. between the two evaluation points, are not reported for simplicity; in the top part of Figure 1 they are compared to the exact and to the two-node beam element solution.

### 5.4 Results Analysis

The top part of Figure 1 compares the tip displacement obtained for unit flexural ( $EJ = 1$ ) and shear ( $GA = 1$ ) stiffness. The flexural displacement of the two-node beam differs from the analytical one even when the force is applied at the beam tip, while the three-node beam recovers the exact solution. Due to the finite-volume formulation, the tip displacement and rotations are null until the force reaches the influence zone of the first unclamped node. The bottom part of Figure 1 compares the tip rotation obtained for unit flexural stiffness. In this case, even the two-node beam recovers the exact rotation when the force is applied at the beam extremities. The internal forces and moments are always recovered exactly at the evaluation points.

In order to trim off the unphysical high frequency transients, related to the finite volume approach and to the spatial discretization of the model, that are introduced each time the slider passes from the influence zone of a node to that of another, the slider reaction force can be “smeared” over a finite length. This not only cures a potentially critical numerical behavior, but also allows to take into account the effective finite dimension of a bearing. Figure 2 reports the internal shear force and the tip displacement of a three-node beam element when a sliding body crosses an evaluation point with a finite, constant velocity. Its left hand part shows how, in absence of smearing, the internal shear grows instantaneously from zero to its unit value with some slight high-frequency oscillations related to the sudden switching of the slider reaction force from one node to the other. Some limited smearing, 1% of the element length, cures the problem without appreciably altering the force distribution; of course, the higher the smearing level, the wider the force distribution. Notice that, if an ideally punctual constraint is envisaged, the smearing introduces some non-causality in the element behavior; however, from a practical point of view, the smearing accounts for the finite size of the cursor and, as such, it can be tuned accordingly. The right hand part of Figure 2 shows the tip displacement of the beam element, normalized by  $EJ/L^3$ , with different smearing values. Note that no smearing introduces a jump with sharp oscillations, while excessive smearing leads to a highly non-causal behavior. On the contrary, a limited smearing effect dramatically reduces the oscillations. As expected, all the solutions converge to a very close behavior after the effects of the smearing disappear, e.g. when the cursor leaves the neighborhood of the evaluation point.

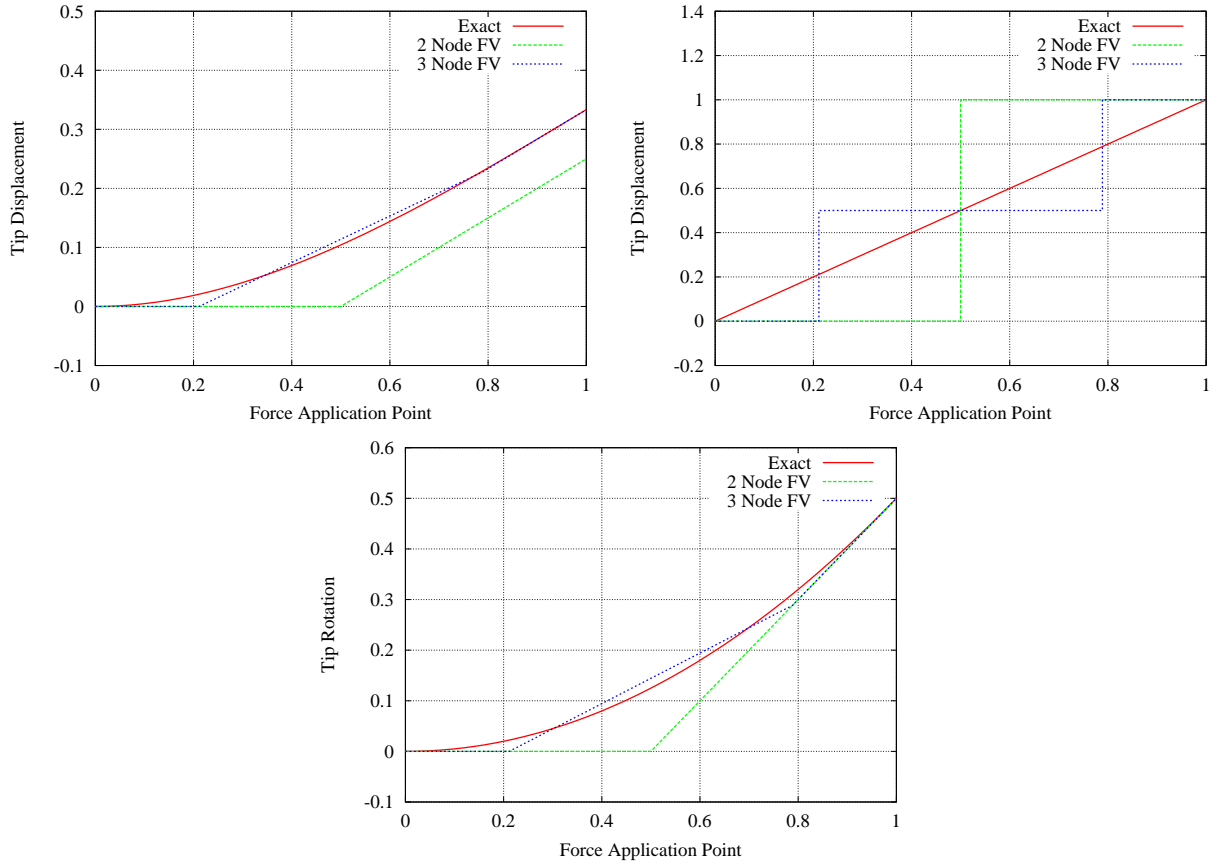


Figure 1: Flexural (top, left) and Shear (top, right) Part of Tip Displacement; Tip Rotation (bottom)

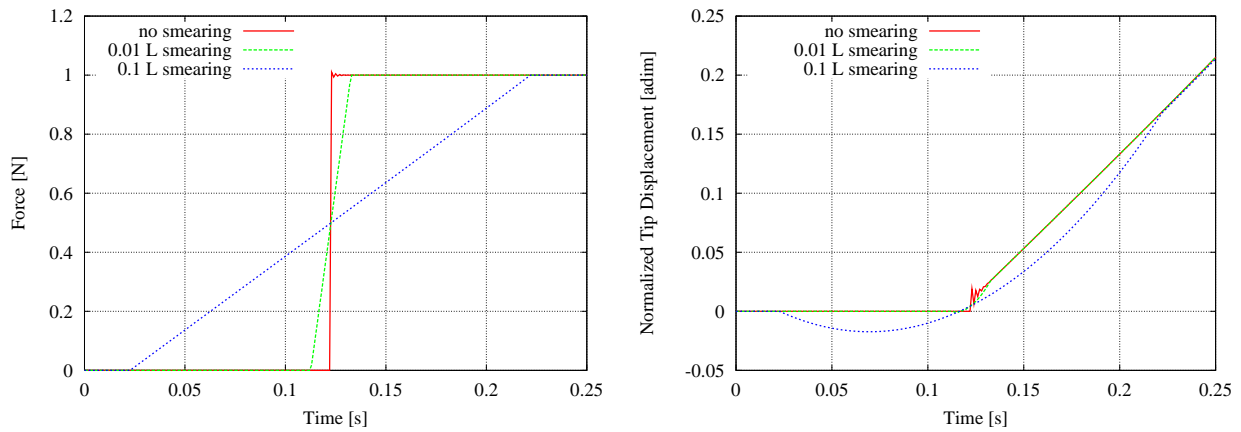


Figure 2: Internal Shear (left) and Tip Displacement (right) with Increasing Smearing Levels

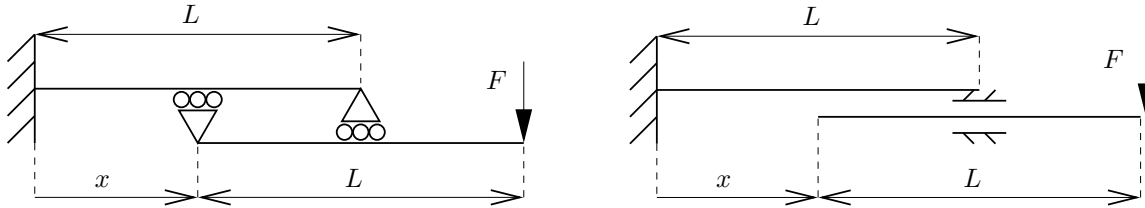


Figure 3: Sliding Beams Setup

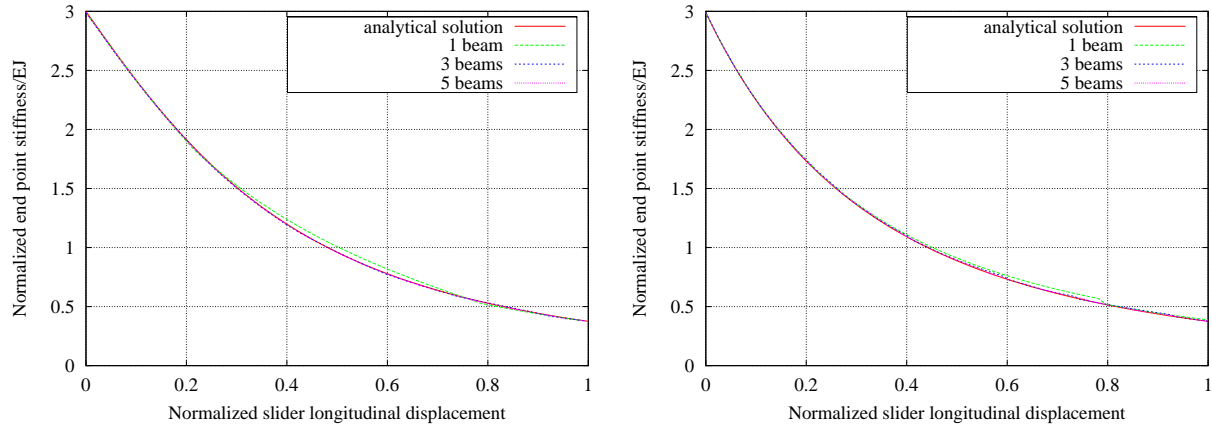


Figure 4: “Spherical”/“Classical” Slider End-Point Stiffness

## 6 Numerical Results

To check the influence of the errors due to the finite volume discretization, highlighted in Par. 5, a simple structural model (Figure 3), with dimensions and stiffnesses comparable to those of a real piston-cylinder arrangement, is analyzed. In Figure 4, the numerical results obtained with 1, 3, and 5 three-node beams for each sliding element are compared to the analytical results obtained for two beams. The tip stiffness,  $F/v(x+L)$ , normalized by  $EJ/L^3$ , is plotted as a function of the normalized slider displacement,  $x/L$ . While the 3 and 5 element solutions are practically undistinguishable from the analytical solution, the single beam element solution differs slightly. The numerical results were obtained for  $EJ = 4.1e4 \text{ Nm}^2$ ,  $GA = 1.1e8 \text{ Nm}^2$  and  $L = 0.6 \text{ m}$ .

Figure 5 shows the detailed tip stiffness relative error for each configuration. Note that both slider models show angular points in the stiffness curve at the evaluation points, where the load is transferred between adjacent nodes. The “classical” slider, which also constrains rotations, shows other angular points at the inter-element nodes, because the beam rotations are  $C^0$  and thus are not regular at the element boundaries. The relative error, with 3 and 5 beam elements, never exceeds 2% and 2.5%, respectively; for a reasonable operating range (0 to 0.8 L), 1% and 1.5% is never exceeded for the “spherical” and the “classical” slider respectively. When a single beam element is used, the largest error is about 5–7%. The static results are only marginally influenced by the choice of the “smearing” length value.

## 7 Landing Gear Application

Previous works in the field of landing gear dynamics simulation have highlighted the fact that the variation of leg bending characteristics on typical telescopic gear during closure cannot be overlooked. Different approaches to the problem have been proposed. Some authors interpolates strut bending behaviour between different, known configurations [7, 10], while others employ specially devised flexible sliding elements [6]; this is the approach adopted here.

The example presented in this paper is a simple telescopic nose landing gear for a general aviation aircraft,

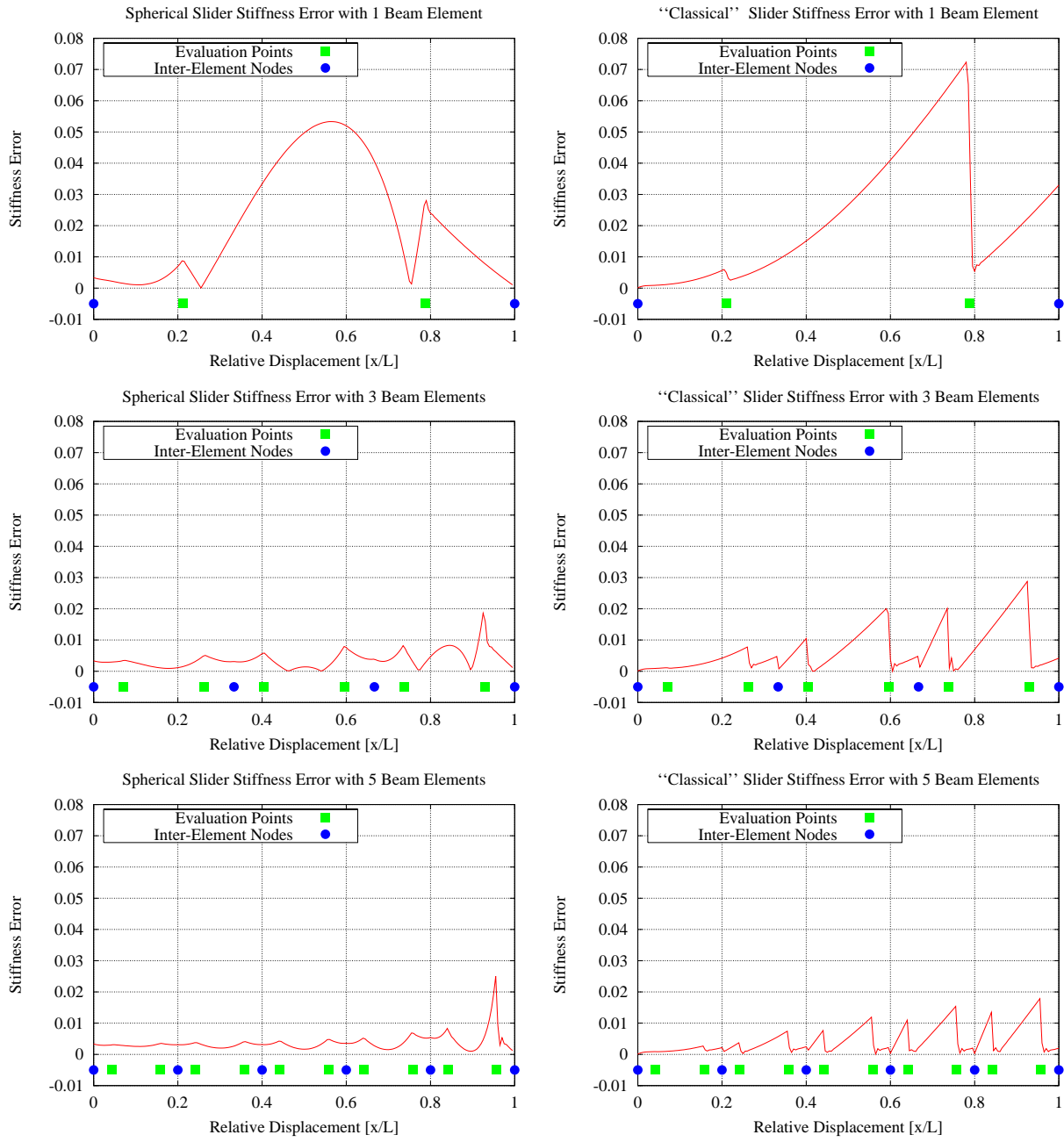


Figure 5: “Spherical”/“Classical” Slider End-Point Stiffness Relative Errors

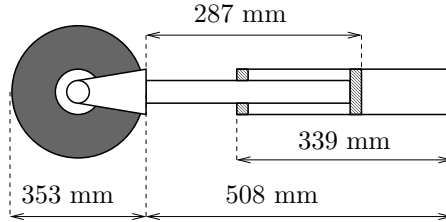


Figure 6: Landing Gear Layout

subjected to spin-up and spring-back loads during the landing maneuver, with an equivalent mass of about 300 kg, a vertical speed of 2.8 m/s and a longitudinal speed of 40 m/s. These loads originate from the fact that the tire peripheral speed at contact differs from the aircraft longitudinal speed. Thus, while the wheel spins up, large longitudinal loads are applied to the system. Once the correct speed is reached, this load ceases and the structure springs back. The landing gear configuration is analogous to that of the nose landing gear described in [5] and [11]; the same shock absorber and tire modeling approaches are used.

Figure 4 shows how the stiffness of the telescoping strut varies during closure: this obviously influences spin-up and spring-back dynamics, as already highlighted in earlier works [7, 10, 6]. The resulting loads cannot be neglected, as is evident in Figure 7, since the peak vertical loads in this condition are about 13000 N. The figure also shows that the dynamics of the piston-cylinder arrangement is negligible with respect to that of the whole landing gear, since the results with 1, 3 and 5 beam elements are practically undistinguishable. A rigid body model cannot capture the spring-back loads, although the peak spin-up loads are only slightly underestimated, as appears by comparing the longitudinal loads computed with a rigid leg.

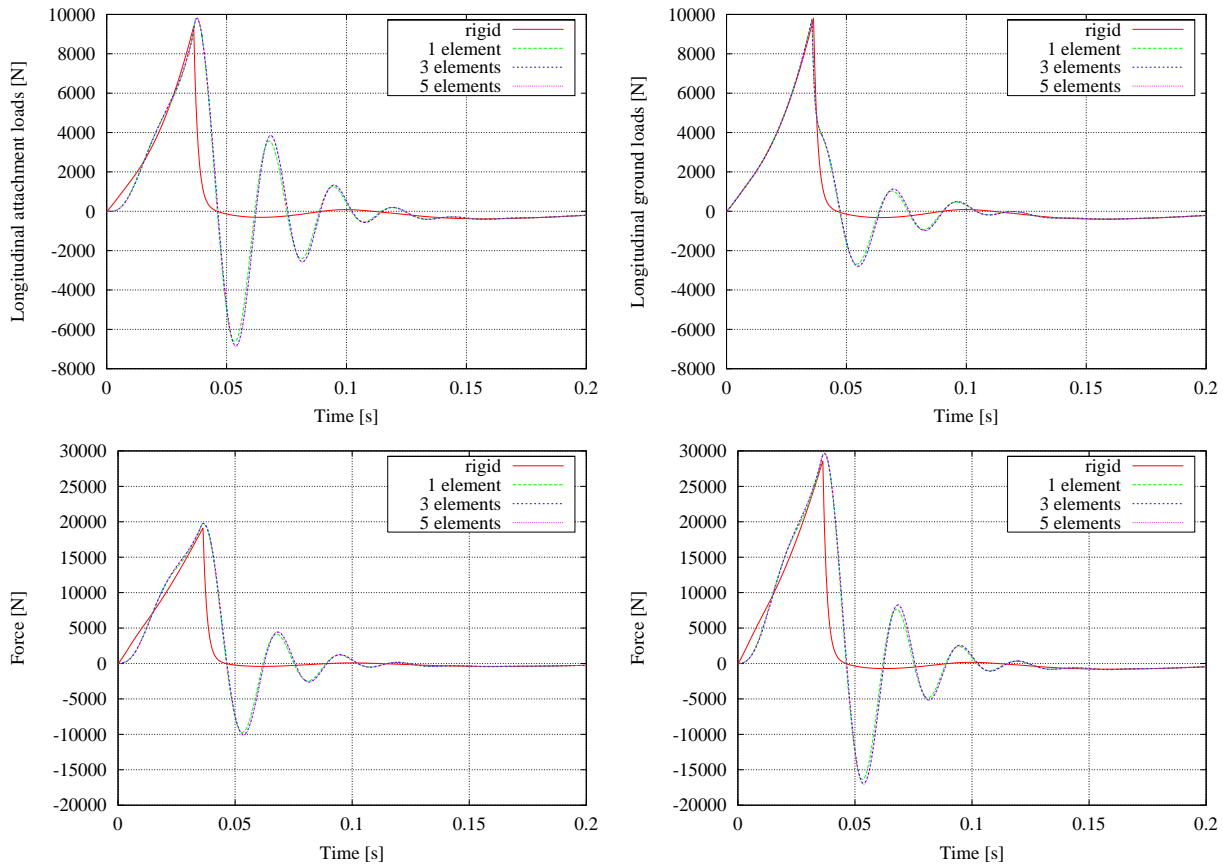


Figure 7: Longitudinal Attachment (top, left), Ground (top, right), Top Slider (bottom, left) and Bottom Slider (bottom, right) Load Time History

The correct simulation of the relative motion between the piston and cylinder of the shock absorber will allow, after the introduction of adequate friction models, the complete simulation of spin-up and spring-back landing phenomena within the MBDyn framework. This aspect is fundamental, because assuming an average 0.02 bearing dynamic friction coefficient, the total peak friction force acting along the strut is in the order of 8–10% of the overall vertical peak force. Applications to the analysis of the shimmy phenomenon are also envisaged.

## 8 Conclusions

A deformable slider joint has been formulated and coupled to a finite volume beam element in the MBDyn multibody/multidisciplinary dynamics analysis framework. Numerical aspects of the implementation have been addressed. The slider constraint has been applied to the modeling of a general aviation aircraft telescopic nose landing gear, and the resulting longitudinal loads have been discussed in comparison with those obtainable from a rigid model.

## References

- [1] O. A. Bauchau. On the modeling of prismatic joints in flexible multi-body systems. *Comput Methods Appl. Mech. Engrg.*, 181:87–105, 2000.
- [2] Gian Luca Ghiringhelli, Pierangelo Masarati, Paolo Mantegazza, and Mark W. Nixon. Multi-body analysis of a tiltrotor configuration. *Nonlinear Dynamics*, 19(4):333–357, August 1999.
- [3] Gian Luca Ghiringhelli, Pierangelo Masarati, and Paolo Mantegazza. Analysis of an actively twisted rotor by multibody global modelling. *Composite Structures*, 52/1:113–122, April 2001.
- [4] Pierangelo Masarati, Paolo Mantegazza, Pierre Abdel Nour, Claudio Monteggia, and Reg Raval. Helicopter control system synthesis by multibody multidisciplinary analysis. In 28<sup>th</sup> *European Rotorcraft Forum*, pages 18.1–12, Bristol, UK, 17–20 September 2002.
- [5] Stefania Gualdi, Pierangelo Masarati, Marco Morandini, and Gian Luca Ghiringhelli. A multibody approach to the analysis of helicopter-terrain interaction. In 28<sup>th</sup> *European Rotorcraft Forum*, pages 72.1–12, Bristol, UK, 17–20 September 2002.
- [6] B. Guyot, P. Thomas, and M. Geradin. Dynamic simulation of landing gears. In *Proceedings of the CEAS Int. Forum on Aeroelasticity and Structural Dynamics*, pages 1077–1095, Strasbourg, France, 24–26 May 1993.
- [7] W. Krüger, I. Besselink, D. Cowling, D. B. Doan, W. Kortüm, and W. Krabacher. Aircraft landing gear dynamics: simulation and control. *Vehicle System Dynamics*, (28):119–158, 1997.
- [8] Gian Luca Ghiringhelli, Pierangelo Masarati, and Paolo Mantegazza. A multi-body implementation of finite volume beams. *AIAA Journal*, 38(1):131–138, January 2000.
- [9] Pierangelo Masarati, Massimiliano Lanz, and Paolo Mantegazza. Multistep integration of ordinary, stiff and differential-algebraic problems for multibody dynamics applications. In *XVI Congresso Nazionale AIDAA*, pages 71.1–10, Palermo, 24–28 Settembre 2001.
- [10] A. Shepherd, T. Catt, and D. Cowling. The simulation of aircraft landing gear dynamics. In *Proceedings of the 18th ICAS Conference*, pages 1317–1327, Beijing, China, 24–26 May 1992.
- [11] Riccardo Bianco-Mengotti, Mario Boschetto, Gian Luca Ghiringhelli, and Stefania Gualdi. Multibody analysis of the dynamic behaviour of a trainer aircraft landing gear. In *XVI Congresso Nazionale AIDAA*, pages 77.1–10, Palermo, 24–28 Settembre 2001.
- [12] S. Yüksel and M. Gürgöze. On the flexural vibrations of elastic manipulators with prismatic joints. *Computers & Structures*, 62(5):897–908, 1997.